Deeply Virtual Compton Scattering off the neutron with the Neutral Particle Spectrometer in Hall C

A. Camsonne, R. Ent, C. Keppel, M. McCaughan, R. Paremuzyan, B. Sawatzky, A. Somov, B. Wojtsekhowski, and C. Zorn

Thomas Jefferson National Accelerator Facility
12000 Jefferson Avenue, Newport News, VA 23606, USA

C. Muñoz Camacho*†, S. Niccolai, and E. Voutier

Laboratoire de Physique des 2 Infinis Irène Joliot-Curie
Université Paris-Saclay, CNRS/IN2P3, IJCLab (Orsay, France)

M. Benali, I. Briki, and M. Mazouz*

Faculté des Sciences de Monastir (Tunisia)

V. Berdnikov, J. Crafts, T. Horn, R. Trotta, and P. Stepanov

The Catholic University of America
Washington, DC 20064, USA

A. Asaturyan, A. Mkrtchyan, H. Mkrtchyan, V. Tadevosyan, H. Voskanyan, and S. Zhamkochyan

A. Alikhanyan National Laboratory, Yerevan Physics Institute, Yerevan 375036, Armenia

M. Amaryan, C. Hyde*, M. Kerver, and C. Ploen

Old Dominion University, Norfolk, VA 23529, USA

P. King, J. Murphy, and J. Roche*

Ohio University, Athens OH 45701, USA

W. J. Briscoe and I. Strakovsky

The George Washington University, Washington, DC 20052, USA

M. Boer

Virginia Polytechnic Institute and State University
Blacksburg, VA 2406, USA

J. R.M. Annand, D. J. Hamilton, and B. McKinnon

University of Glasgow Glasgow G12 8QQ, United Kingdom

* Spokesperson
† Contact person

S. Ali, D. Day, D. Keller, O. Rondon, and J. Zhang

University of Virginia, Charlottesville, VA 22904, USA

K. Brinkmann, S. Diehl, and R. Novotny

Universität Gießen
Luwigstraße 23, 35390 Gießen, Deutschland

D. Dutta

Mississippi State University
Mississippi State, MS 39762, USA

E. Kinney

University of Colorado Boulder, CO 80309, USA

P. Nadel-Turonski

Stony Brook University, Stony Brook, NY

G. Niculescu

James Madison University,
Harrisonburg, VA 22807, USA

S. Sirca

Univerza v Ljubljani, 1000 Ljubljana, Slovenia

I. Albayrak

Akdeniz Üniversitesi, 07070 Konyaalti/Antalya, Turkey

NEUTRAL PARTICLE SPECTROMETER (NPS) COLLABORATION
`https://wiki.jlab.org/cuawiki`

We propose to use the High Momentum Spectrometer of Hall C combined with its Neutral Particle Spectrometer (NPS) to perform high precision measurements of the Deeply Virtual Compton Scattering (DVCS) cross section off quasi-free neutrons in a liquid deuterium (LD_2) target. These data are essential to probe the flavor dependence of the Generalized Parton Distribution (GPDs) of the nucleon. We request 44 days of 3, 4, and 5 pass longitudinally polarized electrons incident on a 10 cm LD_2 target.

Date: May 16, 2022

Contents

I. EXECUTIVE SUMMARY

An exciting scientific frontier is the 3-dimensional exploration of nucleon (and nuclear) structure – nuclear femtography. Jefferson Lab with its high luminosity and expanded kinematic reach at 12-GeV allows detailed investigations of position and momentum distributions of partons inside protons and neutrons in the valence-quark region. The study of Generalized Parton Distributions (GPDs) captures the images of the transverse position distributions of fast-moving quarks. The cleanest reaction to access GPDs is Deeply Virtual Compton Scattering (DVCS): $\gamma^* N \to \gamma N$, measured through the electroproduction of photons: $eN \to e\gamma N$ (with N representing either a proton or a neutron). GPDs enter the DVCS cross section through convolution integrals called Compton Form Factors (CFFs), whose real and imaginary parts can be separated using a polarized electron beam of varying energy and measuring both the helicity-dependent and the helicity-independent DVCS cross sections. Due to the approximate isospin symmetry of QCD, DVCS off quasi-free neutrons allows to determine the contributions from the different quark flavours to the different GDPs by combining proton and neutron DVCS measurements.

An extensive experimental program of DVCS off proton targets is currently approved and ongoing at JLab. We propose to complement this program with an experiment that will measure the cross section of the DVCS reaction off the neutron with high accuracy thanks to the use of the Hall C High Momentum Spectrometer (HMS), the Neutral Particle Spectrometer (NPS) and a LD_2 target. The scattered electron will be detected in the HMS and the emitted photon in the NPS lead tungsten calorimeter. The recoil particle off a deuteron target will be identified by missing mass. The number of events with scattered protons will be computed based on already approved measurements using an LH_2 target. In order to reduce systematic uncertainties, LH_2 and LD_2 run periods should be interleaved frequently (every few hours/days). Recoil neutrons (n) and coherent deuterons (d) are kinematically separated in the missing mass distribution by $\Delta M_X^2 = t(1 - M_n/M_d) \approx t/2$, with t being the momentum transfer to the target.

We propose to exploit the beam energy dependence of DVCS as an additional means to better constraint the experimental extraction of CFFs, a technique that was successfully used on LH_2 targets at 6 GeV [1] and at 12 GeV ([2] and approved E12-13-010).

Helicity-dependent and helicity-independent neutron DVCS cross sections were so far only measured during experiment E08-025 in Hall A before the upgrade of CEBAF to 12 GeV. Results recently published [3, 4] demonstrate the potential of high precision measurements in the flavor separation of CFFs of the nucleon. The extended phase-space enabled by the 11 GeV beam and the upgraded experimental equipment now available will provide multiple advantages for this proposed experiment:

- The higher values of x_B accessible with JLab12 increase the minimum values of t and thus facilitates the separation of neutron DVCS and coherent DVCS off deuterons.
- The contribution of coherent DVCS is also expected to decrease dramatically at higher values of t due to the sharp drop of the deuteron form factors as t increases. This will provide a cleaner identification of the neutron DVCS channel off a deuteron target.
- The higher energy resolution of NPS with respect to the previous measurements using a lead fluoride calorimeter will provide a better missing-mass resolution and thus further enhance the separation of neutron DVCS and coherent DVCS off deuterons.

In summary, the proposed program of precision neutron DVCS cross-section measurements at JLab12 will provide crucial input to the flavor dependence of the nucleon GPDs.

II. INTRODUCTION

Deeply Virtual Compton Scattering (DVCS) refers to the reaction $\gamma^*(q)P(p) \to P(p')\gamma(q')$ in the Bjorken limit of Deep Inelastic Scattering (DIS). Experimentally, we can access DVCS through electroproduction of real photons $e(k)P(p) \to e(k')P(p')\gamma(q')$, where the DVCS amplitude interferes with the so-called Bethe-Heitler (BH) process (Fig. 1). The BH contribution is calculable in QED since it corresponds to the emission of the photon by the incoming or the outgoing electron.

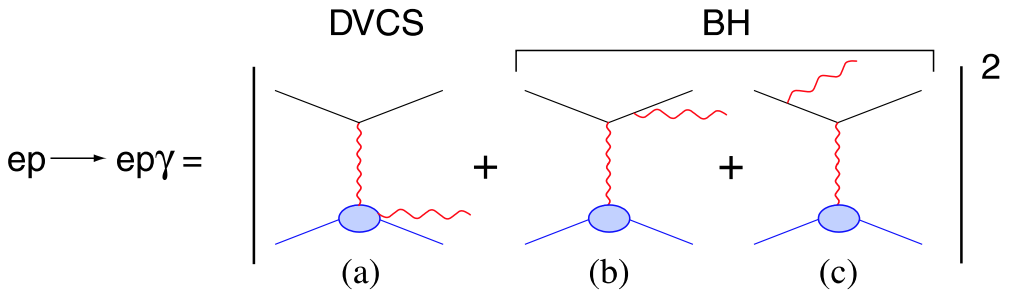

FIG. 1: Illustration of the DVCS (a) and Bethe-Heitler (b and c) processes.

DVCS is the simplest probe of a new class of light-cone (quark) matrix elements, called Generalized Parton Distributions (GPDs). The GPDs offer the exciting possibility of the first ever spatial images of the quark waves inside the proton, as a function of their wavelength [5–10]. The correlation of transverse spatial and longitudinal momentum information contained in the GPDs provides a new tool to evaluate the contribution of quark orbital angular momentum to the proton spin.

A factorization theorem has been proven for DVCS in the Bjorken limit [11, 12]. It allows one to compute the DVCS amplitude as the product of some GPDs and corresponding coefficient functions that can be calculated perturbatively. GPDs are thus in very solid theoretical footing: at leading-twist level, all-order QCD-factorization theorems directly relate the GPDs to particular hard exclusive scattering processes. Therefore, GPDs are process-independent, universal quantities.

GPDs enter the DVCS cross section through integrals over the quark momentum fraction x, called Compton Form Factors (CFFs). CFFs are defined in terms of the vector GPDs H and E, and the axial vector GPDs $\widetilde{H}$ and $\widetilde{E}$. For example ($f \in \{u, d, s\}$) [13]:

$$\mathcal{H}(\xi,t) = \sum_f \left[\frac{e_f}{e}\right]^2 \left\{ i\pi \left[H_f(\xi,\xi,t) - H_f(-\xi,\xi,t)\right] + \mathcal{P}\int_{-1}^{+1} dx \left[\frac{1}{\xi - x} - \frac{1}{\xi + x}\right] H_f(x,\xi,t) \right\}, \quad (1)$$

where $t = (p - p')^2$ is the momentum transfer to the nucleon and skewness variable ξ is defined as $\xi = -\overline{q}^2/(\overline{q}\cdot\overline{p}) \approx x_{\rm B}/(2 - x_{\rm B})$, with $\overline{q} = (q + q')/2$ and $\overline{p} = p + p'$. Thus, the imaginary part of a CFF accesses a GPD along the line $x = \pm\xi$, whereas the real part probes GPD integrals over x. The 'diagonal' GPD, $H(\xi, \xi, t = \Delta^2)$ is not a positive-definite probability density, however it is a transition density with the momentum transfer $\Delta_\perp$ Fourier-conjugate to the transverse distance r between the active parton and the center-of-momentum of the spectator partons in the target [14]. Furthermore, the real part of the CFF is determined

by a dispersion integral over the diagonal $x = \pm\xi$ plus the D-term [15–18]:

$$\Re\mathrm{e}\left[\mathcal{H}(\xi,t)\right] = \int_{-1}^{1} dx \left\{ \left[H(x,x,t) + H(-x,x,t)\right] \left[\frac{1}{\xi - x} - \frac{1}{\xi + x}\right] + 2\frac{D(x,t)}{1-x} \right\} \qquad (2)$$

The D-term [19] only has support in the region $|x| < \xi$ in which the GPD is determined by $q\bar{q}$ exchange in the t-channel.

In previous experiments (E03-106, E08-025), we have demonstrated the capability of extracting the coherent $n(e,e'\gamma)n$ signal from incoherent deeply virtual Compton scattering (DVCS) on a deuterium target: $D(e,e'\gamma)X$ [3, 4, 20]. After the subtraction of accidentals and the π^0 background, the remaining events in the exclusive region can be statistically identified, within the impulse approximation, as the sum of coherent elastic events $d(e,e'\gamma)d$ and two incoherent quasi-elastic channels:

$$D(e,e'\gamma)X = d(e,e'\gamma)d + n(e,e'\gamma)n + p(e,e'\gamma)p, \qquad (3)$$

where $X = np \oplus d$. The quasi-free $p(e,e'\gamma)p$ contribution is determined by normalizing the LH_2 data to the luminosity of the LD_2 data and by convoluting event-by-event the Fermi-momentum [21] of bound protons inside the deuteron. The width variation of the M_X^2 distribution due to the Fermi-momentum smearing is less than 1% and thus its uncertainty negligible on the final results. Figure 2 (bottom) shows the result of the subtraction of the (background-subtracted) LH_2 signal from the LD_2 data in experiment E08-025 [3]. The resulting events passing the M_X^2 exclusivity selection criterion correspond to the $d(e,e'\gamma)d$ and $n(e,e'\gamma)n$ channels, which are kinematically separated by $\Delta M_X^2 = t(1 - M_n/M_d) \approx t/2$. While the two channels are partially overlaping, which create correlations in the extraction of the individual contributions, the cross sections of both neutron DVCS and coherent deuteron DVCS were extracted and shown in Fig. 3.

We can observe that statistically significant values of both neutron and coherent deuteron DVCS were measured beyond the respective BH contributions. The statistical uncertainties are dominated by correlations in the separation of both channels, which will be highly improved in the proposed experiment herein as we will argue and show below.

By combining the measured neutron cross sections with those measured at the same kinematics using a proton target, a flavor separation of the real and imaginary parts of helicity-dependent CFFs $\mathcal{H}$, $\widetilde{\mathcal{H}}$ and $\mathcal{E}$ was performed and displayed in Fig. 4, which demonstrate the potential of high precision measurements on the neutron to probe the flavor dependence of GPDs.

III. PROPOSED MEASUREMENTS AND MOTIVATION

A. Energy dependence of the DVCS cross section

The photon electroproduction cross section of a polarized lepton beam of energy k off an unpolarized target of mass M is sensitive to the coherent interference of the DVCS amplitude with the Bethe-Heitler amplitude (see Fig. 5). It can be written as:

$$\frac{d^5\sigma(\lambda,\pm e)}{d^5\Phi} = \frac{d\sigma_0}{dQ^2 dx_B} \left|\mathcal{T}^{BH}(\lambda) \pm \mathcal{T}^{DVCS}(\lambda)\right|^2 / |e|^6$$

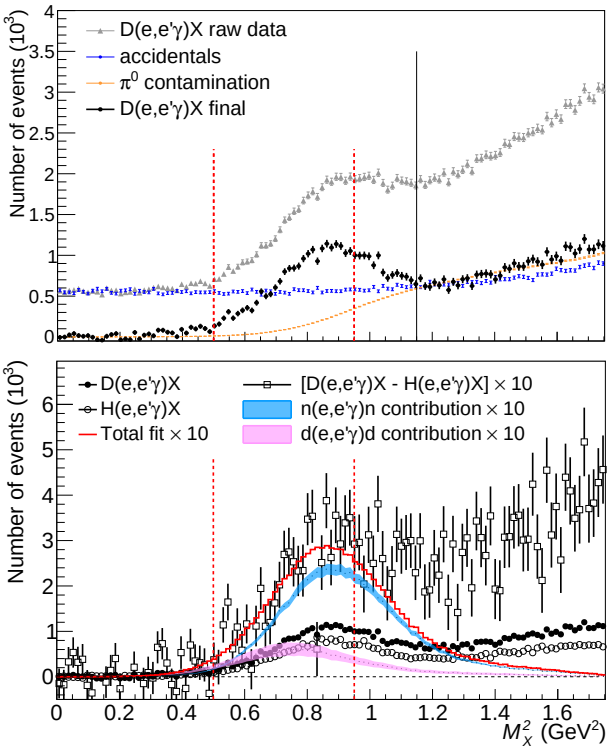

FIG. 2: Missing mass squared distributions from [3]. (Top) The grey triangles show the raw data distribution of $\mathrm{D}(e,e'\gamma)X$ for $E = 4.45$ GeV and the bin $\langle t \rangle = -0.32$ GeV^2, integrated over ϕ. The contributions of accidentals and π^0 contamination are shown in blue and orange respectively. The subtraction of these two contributions from the raw spectrum yields the black circles histogram (also shown in the bottom plot). The pion production threshold is represented by the solid vertical line at 1.15 GeV^2. The range in $M_X^2 \in [0.5, 0.95]$ GeV^2 used in the analysis is shown by the dashed vertical lines. (Bottom) The difference between the $\mathrm{D}(e,e'\gamma)X$ (black circles) and normalized Fermi-smeared $\mathrm{H}(e,e'\gamma)X$ events (white circles), after accidental and π^0 background subtraction, is shown by the white squares histogram (scaled by a factor 10 for clarity). The blue and magenta bands (both scaled $\times 10$), show the simulated $n(e,e'\gamma)n$ and $d(e,e'\gamma)d$ yields, respectively, fit to the data. These bands include the s.d. statistical uncertainty of the fit. The total fit to the white squares distribution is shown by the red histogram.

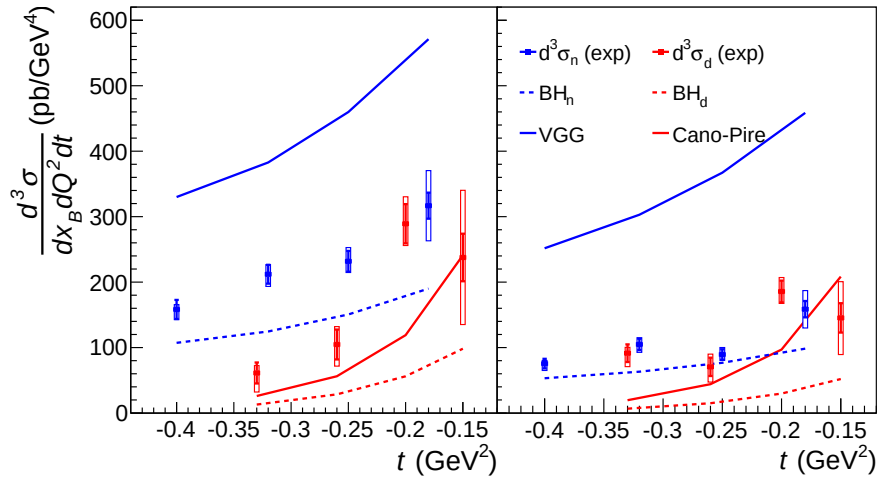

FIG. 3: Neutron and deuteron cross sections integrated over ϕ [3]. The blue (red) points correspond to the $en \to en\gamma$ ($ed \to ed\gamma$) experimental cross sections $d^3\sigma_{n(d)}/dQ^2 dx_B dt$ for beam energy $E = 4.45$ GeV (left) and $E = 5.55$ GeV (right). The error-bars show the s.d. statistical uncertainty and the boxes around the points show the total s.d. systematic uncertainty. Respective BH contributions are shown by the dashed lines, whereas the VGG model [22, 23] for the neutron and Cano-Pire model [24] for the deuteron are represented by the solid curves.

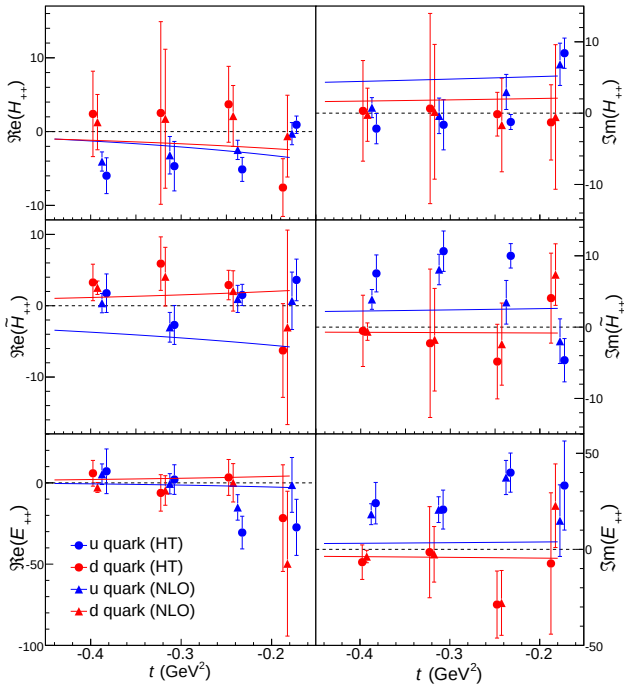

FIG. 4: Flavor separation of helicity-conserved CFFs [3]. The points represent the real (left) and imaginary (right) parts of u (blue) and d (red) helicity-conserved CFFs $\mathcal{H}_{++}$, $\widetilde{\mathcal{H}}_{++}$ and $\mathcal{E}_{++}$ in two scenerios: a fit which also includes single helicity-flip CFFs (labeled HT) and a fit which also includes double helicity-flip CFFs (labeled NLO). The error bars correspond to standard deviations and take into account the statistical and the systematic uncertainties of the fitted cross sections. Solid lines present the predictions of a Reggeized diquark model of GPDs [25, 26].

$$= \frac{d\sigma_0}{dQ^2 dx_B}\left[\left|\mathcal{T}^{BH}(\lambda)\right|^2 + \left|\mathcal{T}^{DVCS}(\lambda)\right|^2 \mp \mathcal{I}(\lambda)\right]\frac{1}{e^6} \tag{4}$$

$$\frac{d\sigma_0}{dQ^2 dx_B} = \frac{\alpha^3_{\rm QED}}{16\pi^2(s_e - M^2)^2 x_B}\frac{1}{\sqrt{1+\epsilon^2}} \tag{5}$$

$$\epsilon^2 = 4M^2 x_B^2/Q^2$$

$$s_e = 2Mk + M^2$$

where $d^5\Phi = dQ^2 dx_B d\phi_e dt d\phi_{\gamma\gamma}$, λ is the electron helicity and the $+(-)$ stands for the sign of the charge of the lepton beam.

The BH contribution is calculable in QED, given our $\approx 1\%$ knowledge of the proton elastic form factors at small momentum transfer. The other two contributions to the cross section, the interference and the DVCS^2 terms, provide complementary information on GPDs. It is possible to exploit the structure of the cross section as a function of the angle $\phi_{\gamma\gamma}$ between the leptonic and hadronic plane to separate up to a certain degree the different contributions to the total cross section [27]. The angular separation can be supplemented by an energy separation. This was the primary goal of approved experiment E12-13-010 on an LH_2 target. We propose to enhance the impact of the LD_2 data of this proposal by also performing measurements at different beam energies.

The $|\mathcal{T}^{BH}|^2$ term is given in [13], Eq. (25), and only its general form is reproduced here:

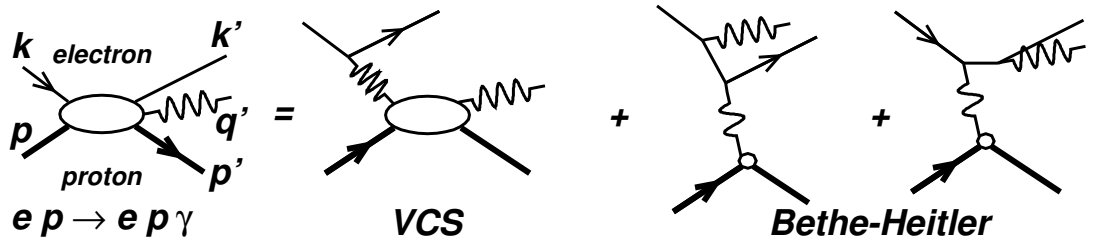

FIG. 5: Lowest order QED amplitude for the $ep \to ep\gamma$ reaction. The momentum four-vectors of all external particles are labeled at left. The net four-momentum transfer to the proton is $\Delta_\mu = (q - q')_\mu = (p' - p)_\mu$. In the virtual Compton scattering (VCS) amplitude, the (spacelike) virtuality of the incident photon is $Q^2 = -q^2 = -(k - k')^2$. In the Bethe-Heitler (BH) amplitude, the virtuality of the incident photon is $-\Delta^2 = -t$. Standard (e, e') invariants are $s_e = (k + p)^2$, $x_{\rm B} = Q^2/(2q \cdot p)$ and $W^2 = (q + p)^2$.

$$|\mathcal{T}^{BH}|^2 \;=\; \frac{e^6}{x_B^2 t y^2 (1+\epsilon^2)^2 \mathcal{P}_1(\phi_{\gamma\gamma})\mathcal{P}_2(\phi_{\gamma\gamma})} \sum_{n=0}^{2} c_n^{BH} \cos(n\phi_{\gamma\gamma}) \tag{6}$$

The harmonic terms c_n^{BH} depend upon bilinear combinations of the ordinary elastic form factors $F_1(t)$ and $F_2(t)$ of the nucleon. The factors $\mathcal{P}_i$ are the electron propagators in the BH amplitude [13].

The interference term in Eq. 4 is a linear combination of GPDs, whereas the DVCS^2 term is a bilinear combination of GPDs. These terms have the following harmonic structure:

$$\mathcal{I} \;=\; \frac{e^6}{x_B y^3 \mathcal{P}_1(\phi_{\gamma\gamma})\mathcal{P}_2(\phi_{\gamma\gamma}) t} \left\{ c_0^{\mathcal{I}} + \sum_{n=1}^{3} \left[c_n^{\mathcal{I}}(\lambda) \cos(n\phi_{\gamma\gamma}) - \lambda s_n^{\mathcal{I}} \sin(n\phi_{\gamma\gamma}) \right] \right\} \tag{7}$$

$$\left|\mathcal{T}^{DVCS}(\lambda)\right|^2 \;=\; \frac{e^6}{y^2 Q^2} \left\{ c_0^{DVCS} + \sum_{n=1}^{2} \left[c_n^{DVCS} \cos(n\phi_{\gamma\gamma}) + \lambda s_n^{DVCS} \sin(n\phi_{\gamma\gamma}) \right] \right\} \tag{8}$$

The $c_0^{DVCS,\mathcal{I}}$ and $(c,s)_1^{\mathcal{I}}$ harmonics are dominated by twist-two GPD terms, although they do have twist-three admixtures that must be quantified by the Q^2-dependence of each harmonic. The $(c,s)_1^{DVCS}$ and $(c,s)_2^{\mathcal{I}}$ harmonics are dominated by twist-three matrix elements, although the same twist-two GPD terms also contribute (but with smaller kinematic coefficients than in the lower Fourier terms). The $(c,s)_2^{DVCS}$ and $(c,s)_3^{\mathcal{I}}$ harmonics stem from twist-two double helicity-flip gluonic GPDs alone. They are formally suppressed by α_s and will be neglected here. They do not mix, however, with the twist-two quark amplitudes. The exact expressions of these harmonics in terms of the quark CFFs of the nucleon are given in [28].

An essential feature of Eqs. (7) and (8) is the incident beam energy dependence (at fixed Q^2, $\nu = Q^2/(2Mx_{\rm B})$):

$$\begin{aligned} \mathcal{I} &\propto 1/y^3 = (k/\nu)^3, \quad \text{and} \\ \left|\mathcal{T}^{DVCS}\right|^2 &\propto 1/y^2 = (k/\nu)^2. \end{aligned} \tag{9}$$

The lepton propagators of Eq. (7) as well as the $(c,s)_n$ harmonics contain additional beam energy dependences. It is one of the goals of this experiment to exploit this energy dependence to separate the interference and DVCS-squared contributions to each of the Fourier terms.

As detailed in [28], at leading twist there are 7 independent GPD terms:

$$\left\{\Re\mathrm{e}, \Im\mathrm{m}\left[\mathcal{C}^{\mathcal{I}}, \mathcal{C}^{\mathcal{I},V}, \mathcal{C}^{\mathcal{I},A}\right](\mathcal{F})\right\}, \qquad \text{and} \qquad \mathcal{C}^{DVCS}(\mathcal{F}, \mathcal{F}^*). \tag{10}$$

The azimuthal $\phi_{\gamma\gamma}$ dependence of the cross section provides 5 independent observables ($\sim$1, $\sim \cos\phi_{\gamma\gamma}, \sim \sin\phi_{\gamma\gamma}$ and $\sim \cos(2\phi_{\gamma\gamma}), \sim \sin(2\phi_{\gamma\gamma})$). The measurement of the cross section at two or more beam energies for exactly the same Q^2, x_{B}, t kinematics, provides the additional information in order to extract all leading twist observables independently. Measurements with three beam energies (where feasible) will reduce the uncertainty of the extracted coefficients and are important because of the complicated energy dependencies of the kinematic coefficients.

B. Q^2 dependence of DVCS observables

GPD measurements at Jefferson Lab rely on the assumption that deep exclusive reactions are well described by their leading twist mechanism. Theoretically this is true at high values of Q^2. The value of Q^2 at which this approximation is valid experimentally needs to be determined and the contributions of higher twists to observables need to be quantified. The Q^2-dependence of cross sections is the most direct way to separate higher twist contributions to DVCS and other exclusive channels.

We propose measurements at several values of Q^2 for each value of x_B and up to high values of Q^2. High Q^2 settings require to place the calorimeter at very small angle and are enabled by the Neutral Particle Spectrometer (NPS) 0.3 Tesla-m sweep magnet between the target and the calorimeter. The proposed measurements will provide stringent tests of the Q^2-dependence of each separated observable in the DVCS cross section.

IV. EXPERIMENTAL SETUP

Figure 6 shows the proposed experimental setup in Hall C. Scattered electrons will be detected in the High Momentum Spectrometer (HMS) and DVCS photons in the lead tungsten calorimeter of the NPS detector system. The NPS is placed in a cantilevered platform on the Super High Momentum Spectrometer (SHMS) carriage to allow for precise and remote rotation around the Hall C pivot.

The energy resolution of the photon detection is the limiting factor of the experiment. Exclusivity of the reaction is ensured by the missing-mass technique and the missing-mass resolution is dominated by the energy resolution of the calorimeter. The higher energy resolution of the lead tungsten calorimeter of NPS compared to the previous DVCS experiments using a lead fluoride calorimeter will improve the missing-mass resolution by a factor of two approximately, as shown by simulations and illustrated in Fig. 7.

In addition, the use of the NPS sweeping magnet allows to reduce charged particle backgrounds in the calorimeter and thus increase the luminosity with respect to previous experiments.

A. Proton DVCS subtraction

The response of the electromagnetic calorimeter crystals shifts over time, primarily due to radiation damage. While to a great extend this is recovered by a time-dependent frequent calibration, a slight miscalibration of the detector translate into a significant systematic

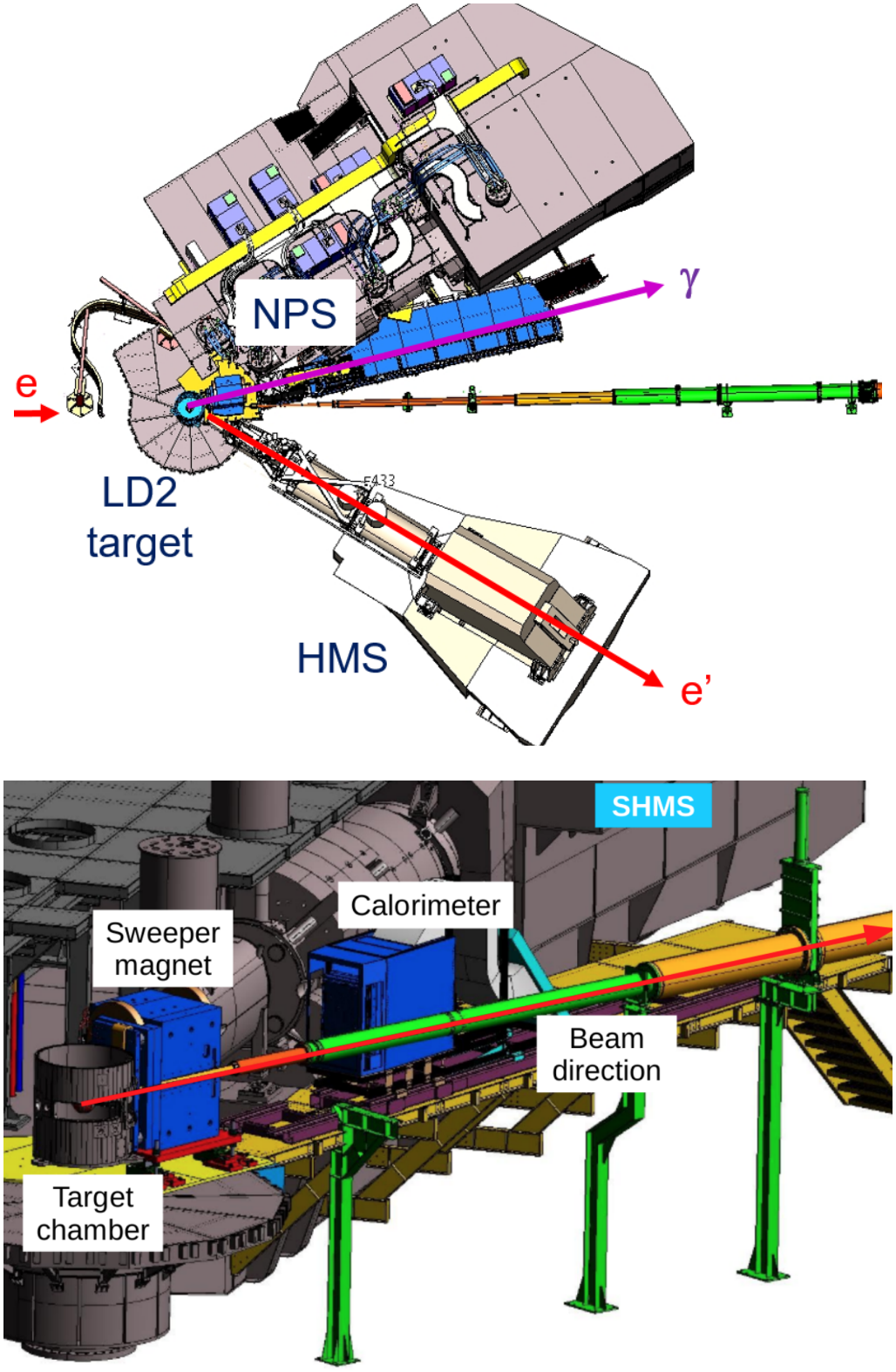

FIG. 6: Experimental setup in Hall C. Top: configuration showing the target chamber and the downstream beam pipe, with the HMS (detecting the scattered electrons) to the beam right and the SHMS to the left of the beam and carrying the NPS sweeping magnet and calorimeter. Bottom: side view of the SHMS carriage that rotates the NPS system (the HMS is not shown in this view).

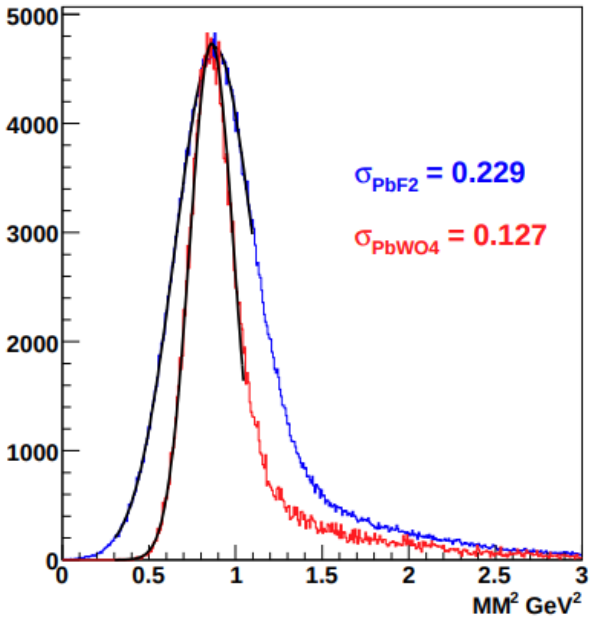

FIG. 7: Projected missing-mass resolution for one of the proposed kinematic settings (E_b = 6.6 GeV^2, Q^2 = 3.0 GeV^2, x_B = 0.36). By using $PbWO_4$ instead of PbF_2 as in previous experiments, the missing-mass resolution will be significantly improved (expected resolution values in each of the settings are provided in Tab. I).

uncertainty when subtracting the proton DVCS events computed with an LH_2 target from events measured with an LD_2 target. To minimize this effect, we propose to interleave the proposed run periods with the LD_2 target with the approved E12-13-010 LH_2 run periods. This will be done at a frequency ranging from several hours to several days, depending on the calorimeter angle, distance and instantaneous luminosity, all factors that affect the radiation damage rate of the crystals. This technique was already successfully applied during experiment E08-025 [3] and greatly improved the analysis with respect to experiment E03-106 [20], in which the helicity-independent cross section could not be measured due to the large systematic uncertainty in the calorimeter relative calibration between the LH_2 and LD_2 runs.

B. Neutral pion detection and background subtraction

Neutral pion $eD \rightarrow e'\pi^0 X$ events will generate both double- $D(e,e'\gamma)\gamma X$ and triple-coincidence $D(e,e'\gamma\gamma)X$ events. The latter events will be used to determine the exclusive π^0 electroproduction cross section. The former are an irreducible background to DVCS, and must be estimated from the latter. The $\pi^0 \rightarrow \gamma\gamma$ decay is isotropic in the pion rest frame. Therefore, with a high statistics sample of $D(e,e'\gamma\gamma)X$ events, it is possible, within a Monte Carlo simulation, to compute an accurate estimate of the background $D(e,e'\gamma)\gamma X$ events. The results of this subtraction procedure is illustrated in Fig. 2 (top) for previous experiment E08-025 [3].

C. GEANT4 simulation

Figure 8 shows the implementation of the experimental setup in GEANT4.

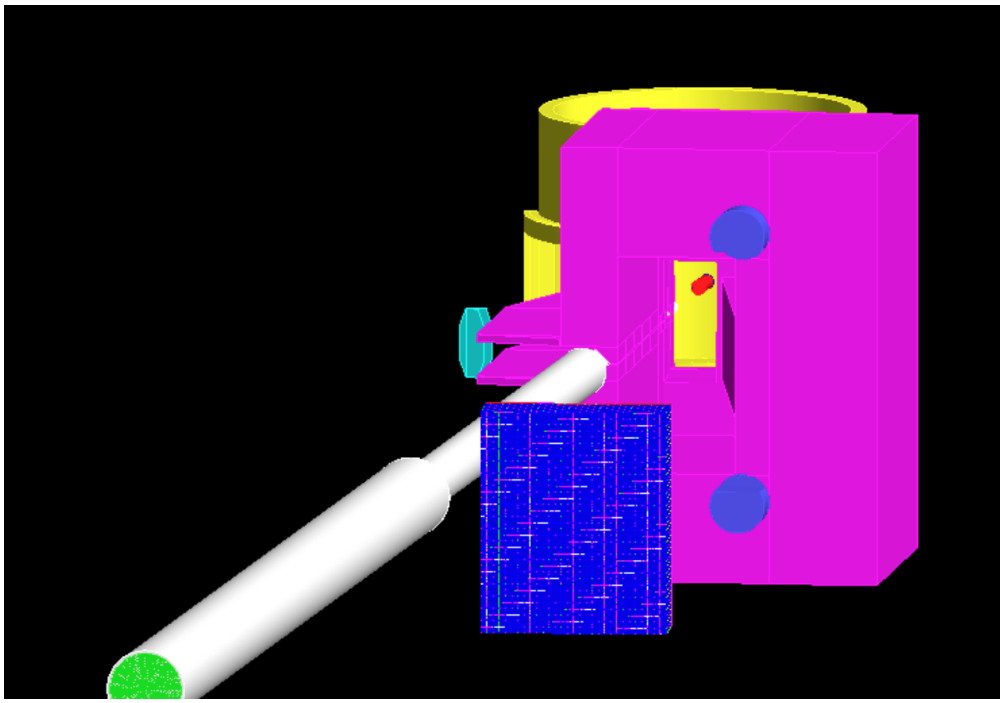

FIG. 8: Implementation of the experimental setup in Geant4: view from the downstream side, showing the outgoing beam pipe, the scattering chamber (yellow) with the LD_2 target inside (red), the sweeping magnet (magenta) and the $PbWO_4$ calorimeter (blue). The entrance window of the HMS is shown in cyan.

Proton DVCS off an LH_2 target and neutron and deuteron DVCS events off an LD_2 target have been simulated through the full Geant4 implementation of the experimental setup. Proton and neutron DVCS events have been weighted by cross sections calculated with the VGG model of GPDs [23]. The coherent deuteron channel is modeled only with the Bethe-Heitler cross section, as we do not currently have access to a full deuterium coherent DVCS code.

In order to optimize the statistical uncertainties on the subtraction of events taken with an LH_2 target, the beam time assumed matches the one approved in experiment E12-13-010 with a proton target.

V. PROJECTIONS

A. Proton DVCS E12-13-010

The approved run plan for proton DVCS experiment E12-13-010 is summarized in Tab. I. We propose to complement this program with matching data runs using an LD_2 target. Tab. I shows the expected missing-mass resolution ($\sigma_{M_X^2}$) in each of the settings, as well as the corresponding minimum value of the momentum transfer $-t_{min}$.

Due to the need to subtract the incoherent proton DVCS contribution from the LD_2 data, the statistical uncertainties are optimized by matching the beam time run in each of

the targets. We do not include in this request the settings with $x_B = 0.2$ due to the poor separation of the neutron and coherent deuteron signals in the missing-mass distribution (see Tab. I), caused by the low value of $-t_{min}$ in those settings.

x_B	0.2				0.36						0.5			0.6			
Q^2 (GeV)^2	2.0			3.0	3.0			4.0		5.5	3.4		4.8	5.1			6.0
E_b (GeV)	6.6	8.8	11		6.6	8.8	11	8.8	11		8.8	11		6.6	8.8	11	
k' (GeV)	1.3	3.5	5.7	3.0	2.2	4.4	6.6	2.9	5.1	2.9	5.2	7.4	5.9	2.1	4.3	6.5	5.7
$\theta_{\rm Calo}$ (deg)	6.3	9.2	10.6	6.3	11.7	14.7	16.2	10.3	12.4	7.9	20.2	21.7	16.6	13.8	17.8	19.8	17.2
$D_{\rm Calo}$ (m)	6	4		6	3			4	3	4	3						
$I_{\rm beam}$ (μA)	11	5	50	11	28			50	28	50	28						
$\sigma_{M_X^2}$ (GeV^2)	0.17			0.22	0.13		0.12	0.15		0.19	0.09		0.11	0.09			
-t_{min} (GeV^2)	0.04				0.16			0.17			0.37		0.39	0.65			0.67
-$t_{min}/(2\sigma_{M_X^2})$	0.1				0.6			0.55		0.4	2		1.7	3.6			3.7
LH_2 Days	1	1	1	1	1	2	1	1	3	5	3	2	5	5	1	5	10
LD_2 Days					1	2	1	1	3	5	3	2	5	5	1	5	10
					This Proposal: 44 days on LD_2												

TABLE I: Approved DVCS kinematics with NPS and an LH2 target (E12-13-010). The incident and scattered beam energies are k and k', respectively. The calorimeter is centered at the angle $\theta_{\rm Calo}$, which is set equal to the nominal virtual-photon direction. The front face of the calorimeter is at a distance $D_{\rm Calo}$ from the center of the target. The values of -$t_{min}/(2\sigma_{M_X^2})$ represent the minimal separation, in units of M_X^2 resolution, between the neutron and coherent deuteron DVCS signals in a M_X^2 spectrum. This value was about 0.4 in the previous E08-025 experiment.

We present below sample projected results for three of the D$(e, e'\gamma)X$ kinematics settings of Tab. I.

B. Example of deuteron quasi-free DVCS kinematics

We show in this section detailed projections for three kinematics settings, one for each value of $x_B = 0.36$, 0.50 and 0.60.

Figures 9–11 display projected results for 1 day of D$(e, e'\gamma)X$ running at setting from Table I with $E_b = 6.6$ GeV, $x_B = 0.36$ and $Q^2 = 3.0$ GeV^2. Figure 9 displays the M_X^2 distribution for each channel. Figure 10 displays the projected event distribution, including NPS acceptance in five bins in $t = (q - q')^2$. Figure 11 shows the projected extracted differential cross sections for $p(e, e'\gamma)p$ (magenta), $n(e, e'\gamma)n$ (blue) and $d(e, e'\gamma)d$ (red).

Figures 12–14 show the corresponding projections for a three day run at $E_b = 8.8$ GeV, $x_B = 0.50$ and $Q^2 = 3.4$ GeV^2. Figs. 15-17 show the corresponding projections for a five day run at $E_b = 11$ GeV, $x_B = 0.60$ and $Q^2 = 5$ GeV^2. Notice that due to the fast drop of the deuteron form factors as $-t$ increases, the projected number of counts for coherent deuteron DVCS is negligible, according to our estimate based only on the BH contribution, in particular at high x_B. However, if the deuteron DVCS signal were to be much larger than the projected one, its separation in the missing-mass distribution would be relatively clean, as illustrated in Figs. 9, 12 and 15.

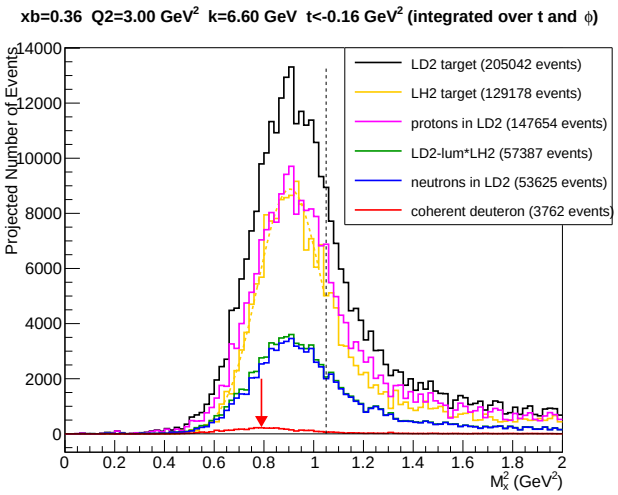

FIG. 9: Projected M_X^2 distribution of $\mathrm{D}(e,e'\gamma)X$ at $E_b = 6.6$ GeV, $x_B = 0.36$ and $Q^2 = 3.0$ GeV^2 (black). The magenta distribution is obtained by Fermi-smearing the signal in a LH_2 target (yellow). The normalized subtraction of the magenta curve from the black histogram yields the green distribution, to which a neutron (blue) and coherent deuteron (red) DVCS signals are fitted. The red arrow indicates the position of the coherent deuteron DVCS signal, separated from the neutron DVCS channel by $\approx t/2$. The projected numbers of events below the M_X^2 cut (vertical dashed line) are shown in the legend.

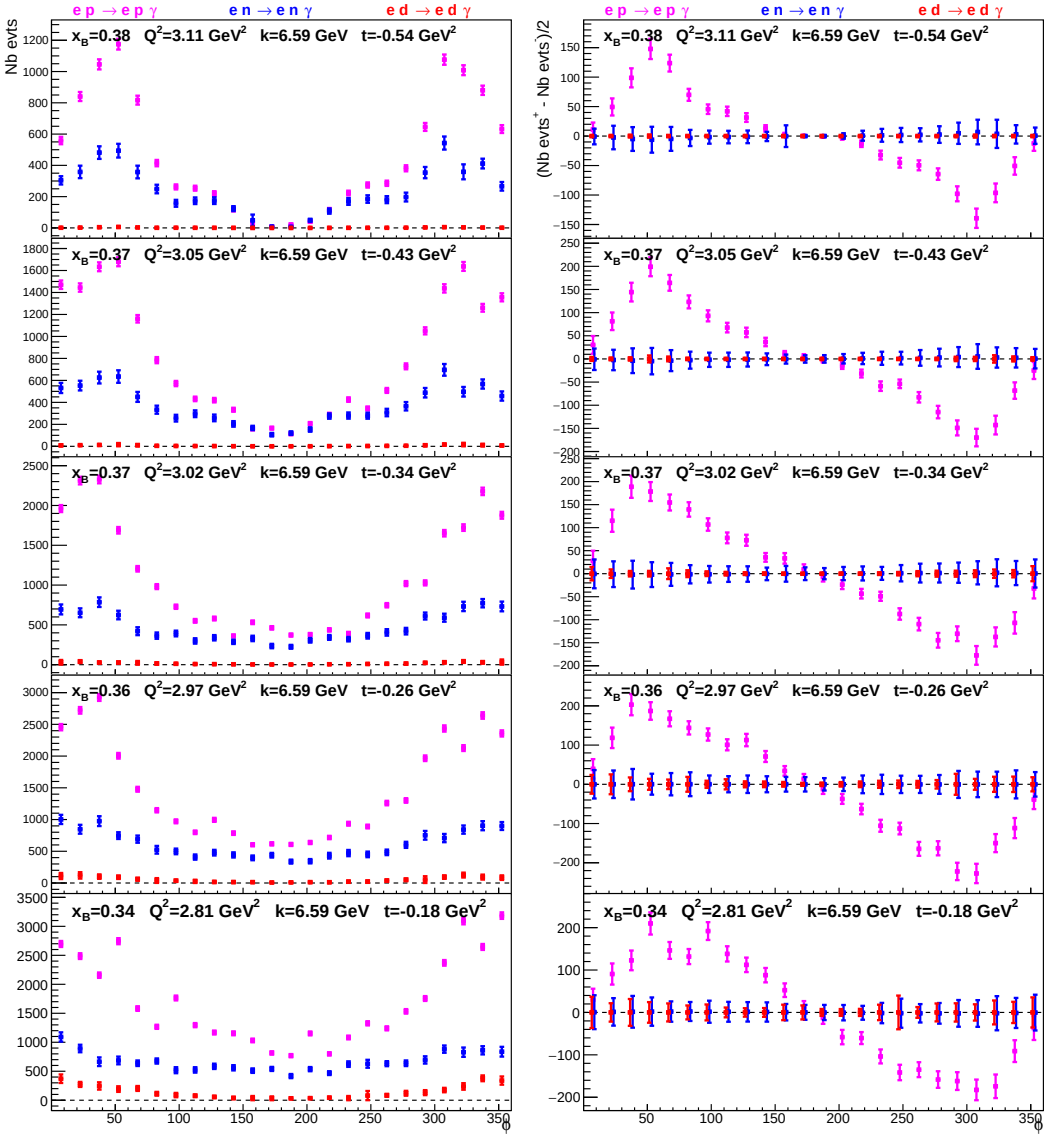

FIG. 10: Projection for event yield of $\mathrm{D}(e,e'\gamma)X$ at $E_b = 6.6$ GeV, $x_B = 0.36$ and $Q^2 = 3.0$ GeV^2 (same kinematics as Fig. 9). Yields are separated into each channel of Eq. (3): $p(e,e'\gamma)p$ (magenta), $n(e,e'\gamma)n$ (blue) and $d(e,e'\gamma)d$ (red). Left: Helicity-independent yields in five bins of t. Right: Helicity-dependent yields in the corresponding t-bins. The value of $-t$ increases from bottom to top. Statistics are for one day.

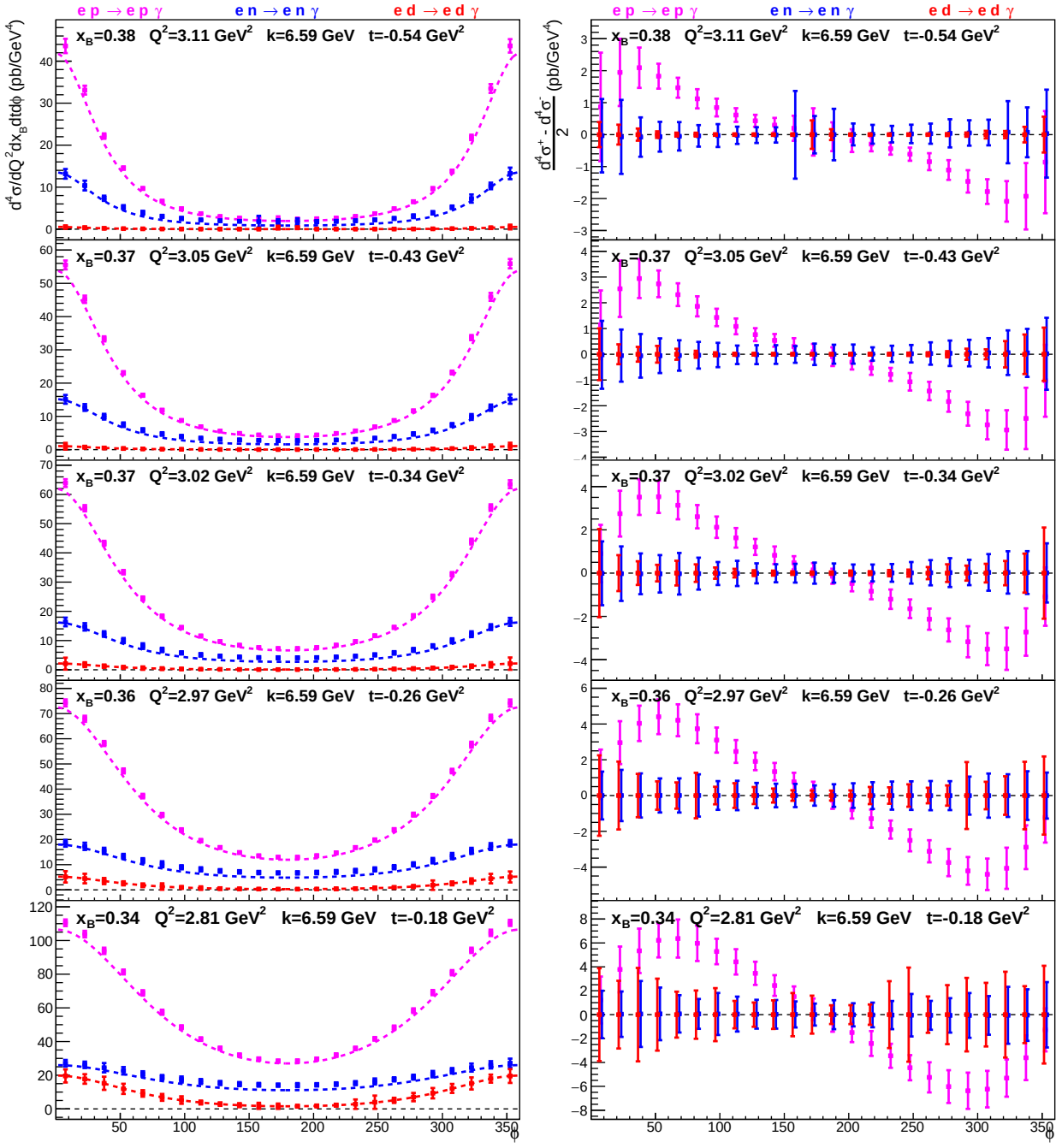

FIG. 11: Projected extracted differential cross sections for D$(e, e'\gamma)X$ at $E_b = 6.6$ GeV, $x_B = 0.36$ and $Q^2 = 3.0$ GeV^2 (same kinematics as Figs. 9, 10). Left: Helicity-independent cross sections. Dashed lines are the pure Bethe-Heitler cross sections for each channel. Right: Helicity-dependent cross sections. Both are in pb/GeV^4. Error bars are statistical uncertainties for one day.

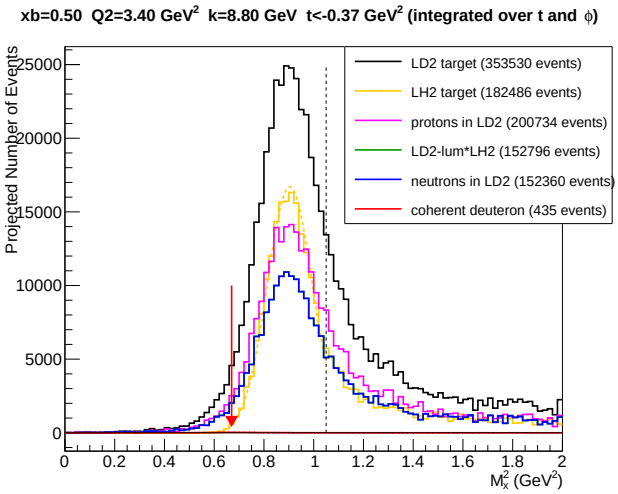

FIG. 12: Projected M_X^2 distribution of $D(e,e'\gamma)X$ at $E_b = 8.8$ GeV, $x_B = 0.50$ and $Q^2 = 3.4$ GeV^2 (black). The magenta distribution is obtained by Fermi-smearing the signal in a LH_2 target (yellow). The normalized subtraction of the magenta curve from the black histogram yields the green distribution, to which a neutron (blue) and coherent deuteron (red) DVCS signals are fitted. The red arrow indicates the position of the coherent deuteron DVCS signal, separated from the neutron DVCS channel by $\approx t/2$. The projected numbers of events below the M_X^2 cut (vertical dashed line) are shown in the legend.

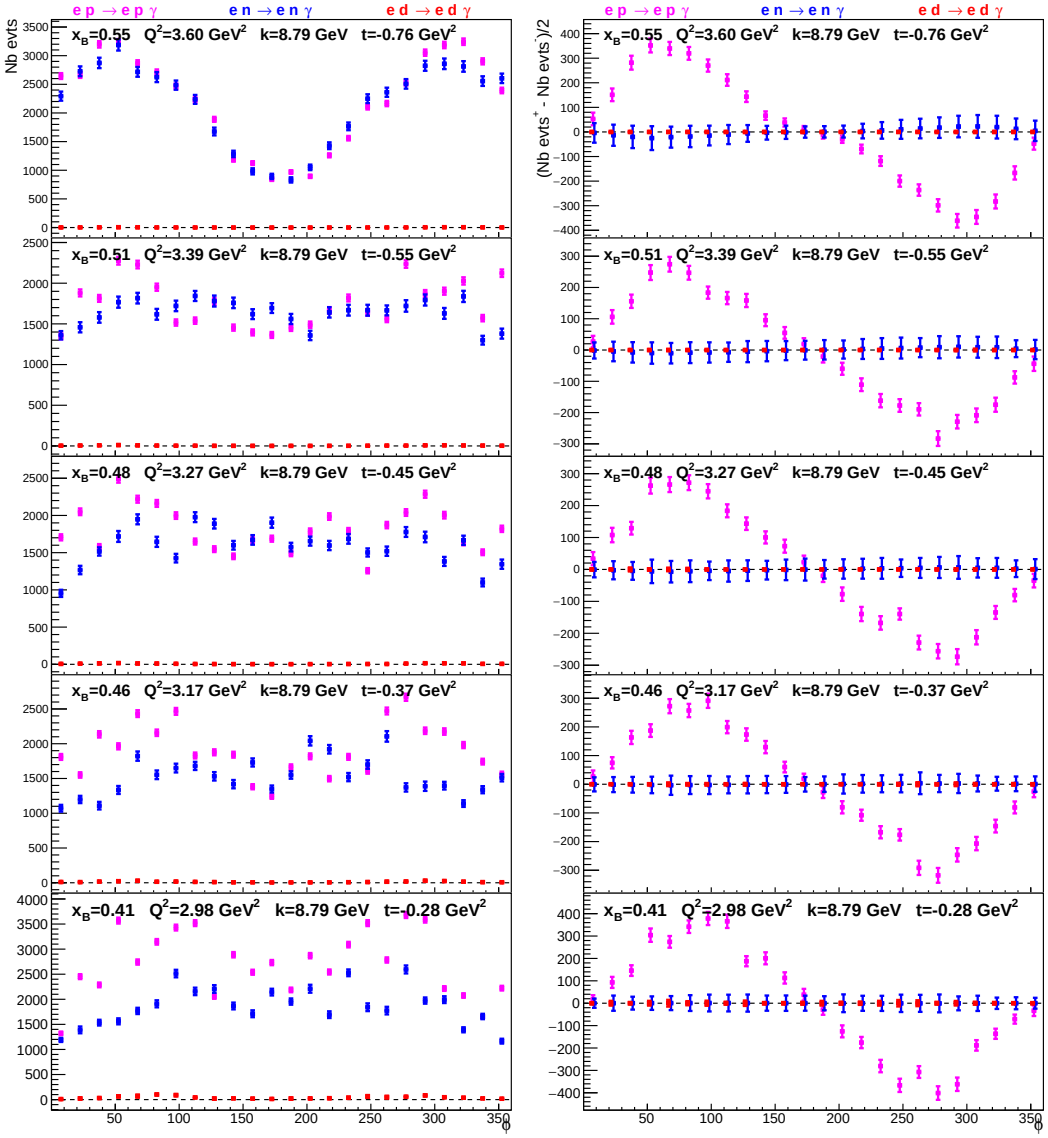

FIG. 13: Projection for event yield of $D(e,e'\gamma)X$ at $E_b = 8.8$ GeV, $x_B = 0.50$ and $Q^2 = 3.4$ GeV^2. Left: Helicity-independent yields in five bins of t. Right: Helicity-dependent yields in the corresponding t-bins. The value of $-t$ increases from bottom to top. Statistics are for 3 days.

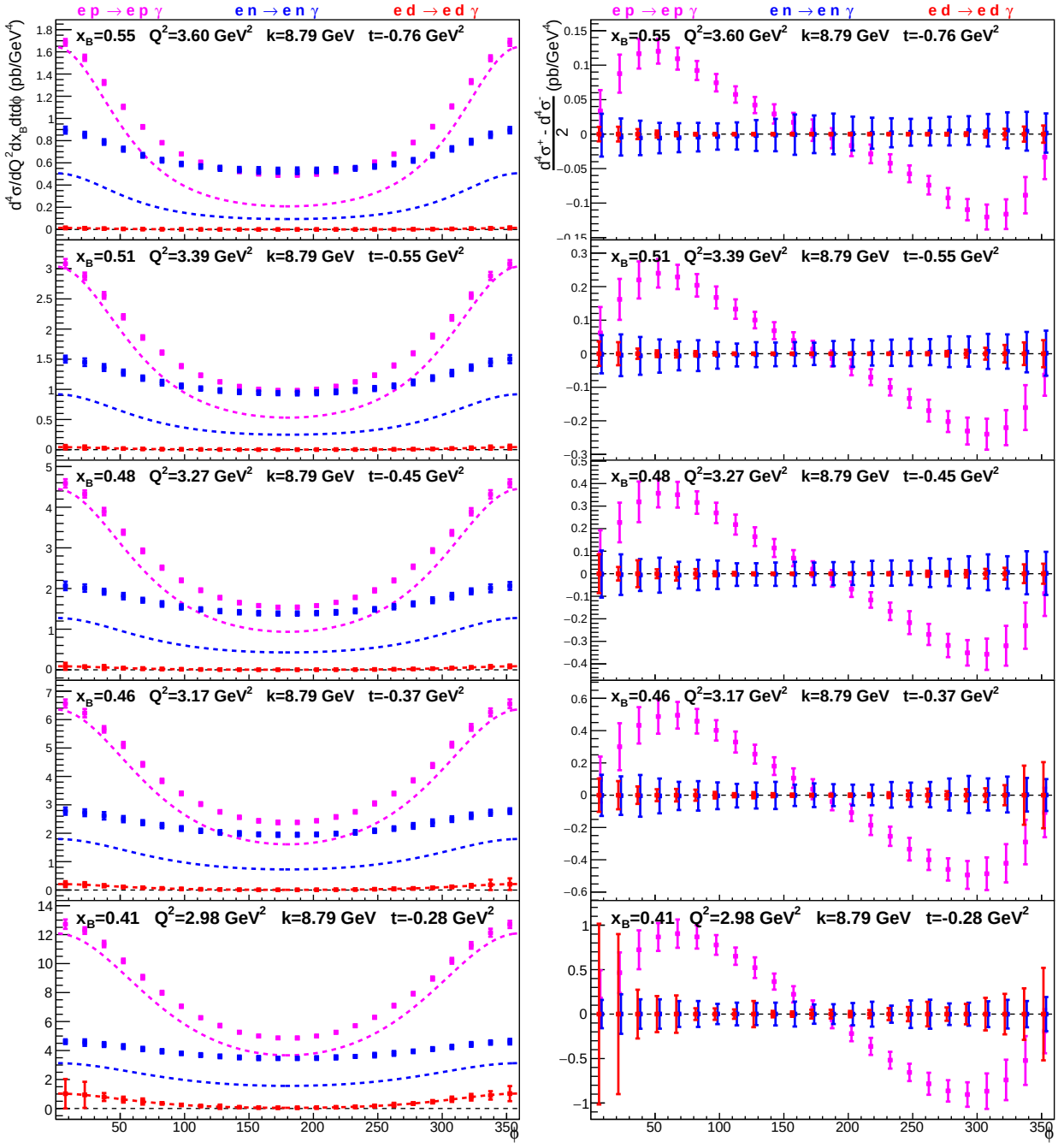

FIG. 14: Projected extracted differential cross sections for D$(e, e'\gamma)X$ at $E_b = 8.8$ GeV, $x_B = 0.50$ and $Q^2 = 3.4$ GeV^2 (same kinematics as Fig. 13). Dashed lines are the pure Bethe-Heitler cross sections for each channel. Left: Helicity-independent cross sections. Right: Helicity-dependent cross sections. Error bars are statistical uncertainties for three days.

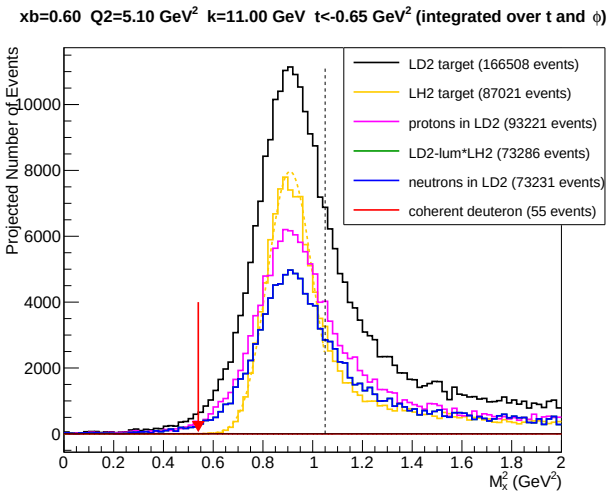

FIG. 15: Projected M_X^2 distribution of $D(e,e'\gamma)X$ at $E_b = 11$ GeV, $x_B = 0.60$ and $Q^2 = 5.1$ GeV^2 (black). The magenta distribution is obtained by Fermi-smearing the signal in a LH_2 target (yellow). The normalized subtraction of the magenta curve from the black histogram yields the green distribution, to which a neutron (blue) and coherent deuteron (red) DVCS signals are fitted. The red arrow indicates the position of the coherent deuteron DVCS signal, separated from the neutron DVCS channel by $\approx t/2$. The projected numbers of events below the M_X^2 cut (vertical dashed line) are shown in the legend.

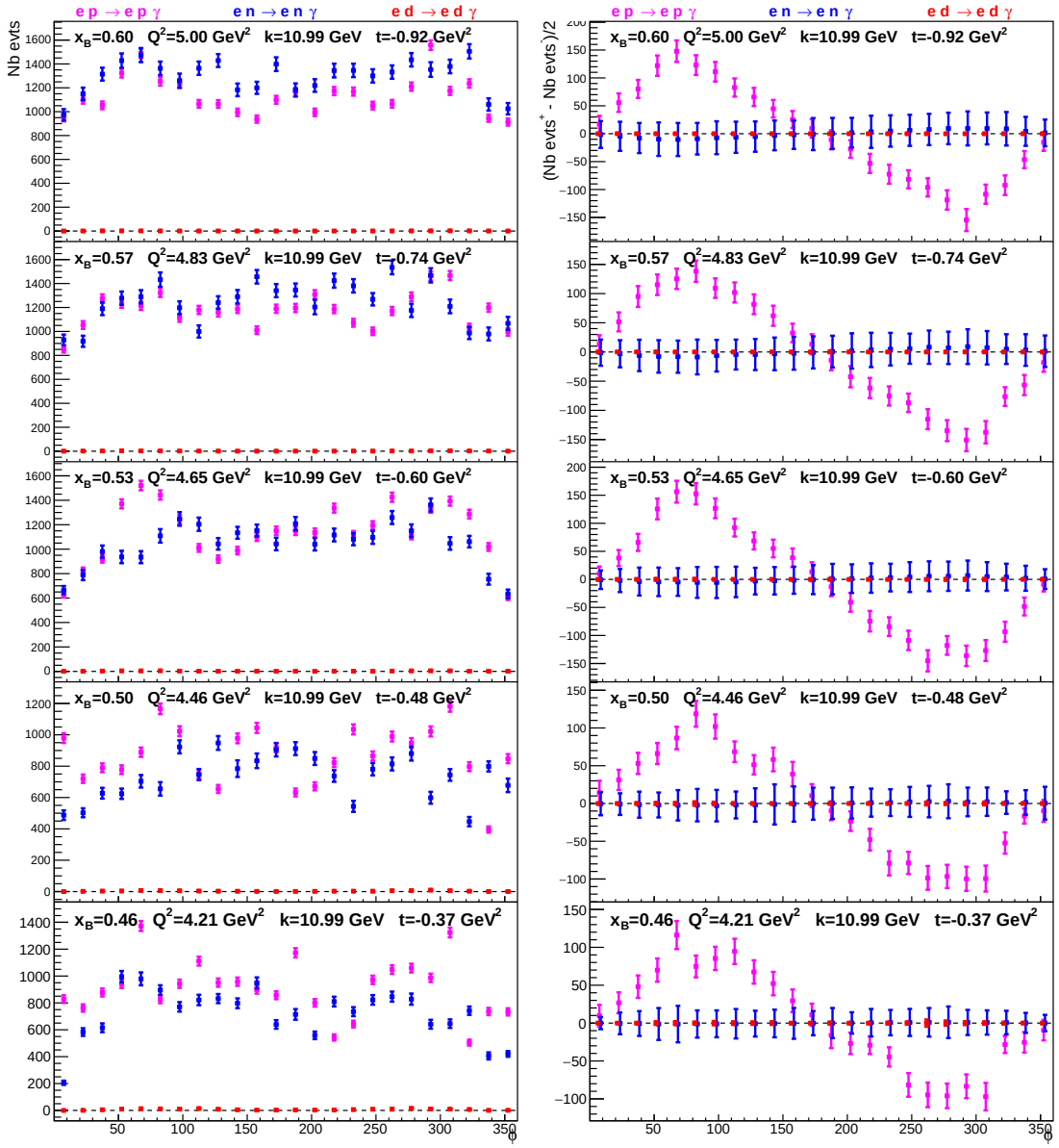

FIG. 16: Projection for event yield of $D(e,e'\gamma)X$ at $E_b = 11$ GeV, $x_B = 0.60$ and $Q^2 = 5.1$ GeV^2. Left: Helicity-independent yields in five bins of t. Right: Helicity-dependent yields in the corresponding t-bins. The value of $-t$ increases from bottom to top. Statistics are for 5 days.

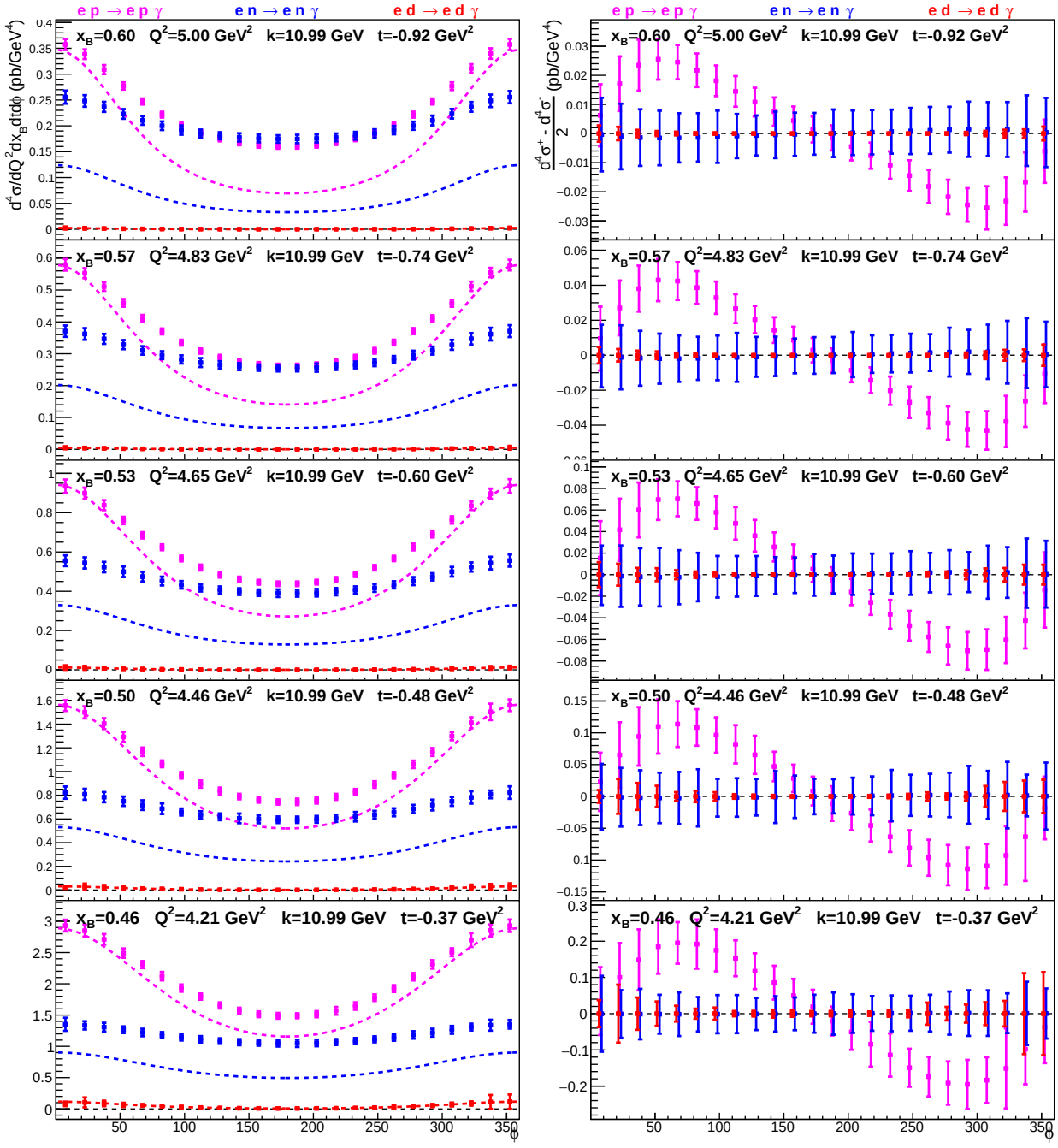

FIG. 17: Projected extracted differential cross sections for $\mathrm{D}(e,e'\gamma)X$ at $E_b = 11$ GeV, $x_B = 0.60$ and $Q^2 = 5.1$ GeV^2 (same kinematics as Fig. 16). Dashed lines are the pure Bethe-Heitler cross sections for each channel. Left: Helicity-independent cross sections. Right: Helicity-dependent cross sections. Error bars are statistical uncertainties for five days.

C. Systematic uncertainties

The HMS is a very well understood magnetic spectrometer which will be used here with modest requirements (beyond the momentum), defining the (x_B, Q^2) kinematics accurately. Table II shows the estimated systematic uncertainties for the proposed experiment based on previous experience from Hall C equipment and Hall A experiments. The uncorrelated errors between high and low ε settings (where ε is the photon polarization parameter) are listed in the first column. The point-to-point uncertainties are amplified by $1/\Delta\varepsilon$ in the beam energy separation. The scale uncertainties propagate directly into the separated cross sections.

Source	pt-to-pt (%)	scale (%)
Acceptance	0.4	1.0
Electron ID	< 0.1	< 0.1
Efficiency	0.5	1.0
Electron tracking efficiency	0.1	0.5
Integrated luminosity	0.5	2.0
Target thickness	0.2	0.5
Kinematics	0.4	< 0.1
Exclusivity	1.0	2.0
π^0 subtraction (for DVCS)	0.5	1.0
Radiative corrections	1.2	2.0
Total	1.8–1.9	3.8–3.9

TABLE II: Estimated systematic uncertainties for the proposed experiment based on previous Hall C and Hall A experiments.

VI. EXCLUSIVE NEUTRAL PION ELECTROPRODUCTION

While DVCS is the main goal of this proposal, exclusive π^0 events will be detected along with DVCS in our experimental setup. Pseudo-scalar mesons provide a very interesting and complementary insight into GPDs of the nucleon. The first cross-section measurements for exclusive π^0 electroproduction in the valence region were performed in Hall A [29] with high precision, and complemented later in a much larger kinematic domain by the CLAS collaboration [30]. Both these datasets were not L/T separated, but provided clear evidence for strong contributions from transversely polarized virtual photons, which was later confirmed by dedicated L/T separations [4, 31] off both proton and quasi-free neutrons (Fig. 18).

This observation is in sharp contrast to the handbag factorization, which tells us that for asymptotically large photon virtualities Q^2, longitudinally polarized photons dominate [32, 33]. According to the handbag approach, the amplitudes for transverse photons are suppressed by $1/Q$ as compared to those from longitudinal photons.

It has been argued in [34, 35] that, within the handbag approach, the π^0 electroproduction amplitudes for transversely polarized virtual photons are determined by transversity GPDs, in particular H_T and $\tilde{E}_T = 2H_T + E_T$ [36, 37]. On the one hand, the amplitudes for transversely polarized photons are parametrically suppressed by μ_π/Q as compared to the asymptotically leading amplitudes for longitudinally polarized photons (related to the usual GPDs $\widetilde{H}$ and $\widetilde{E}$). On the other hand, the parameter μ_π is fixed by the divergence of the

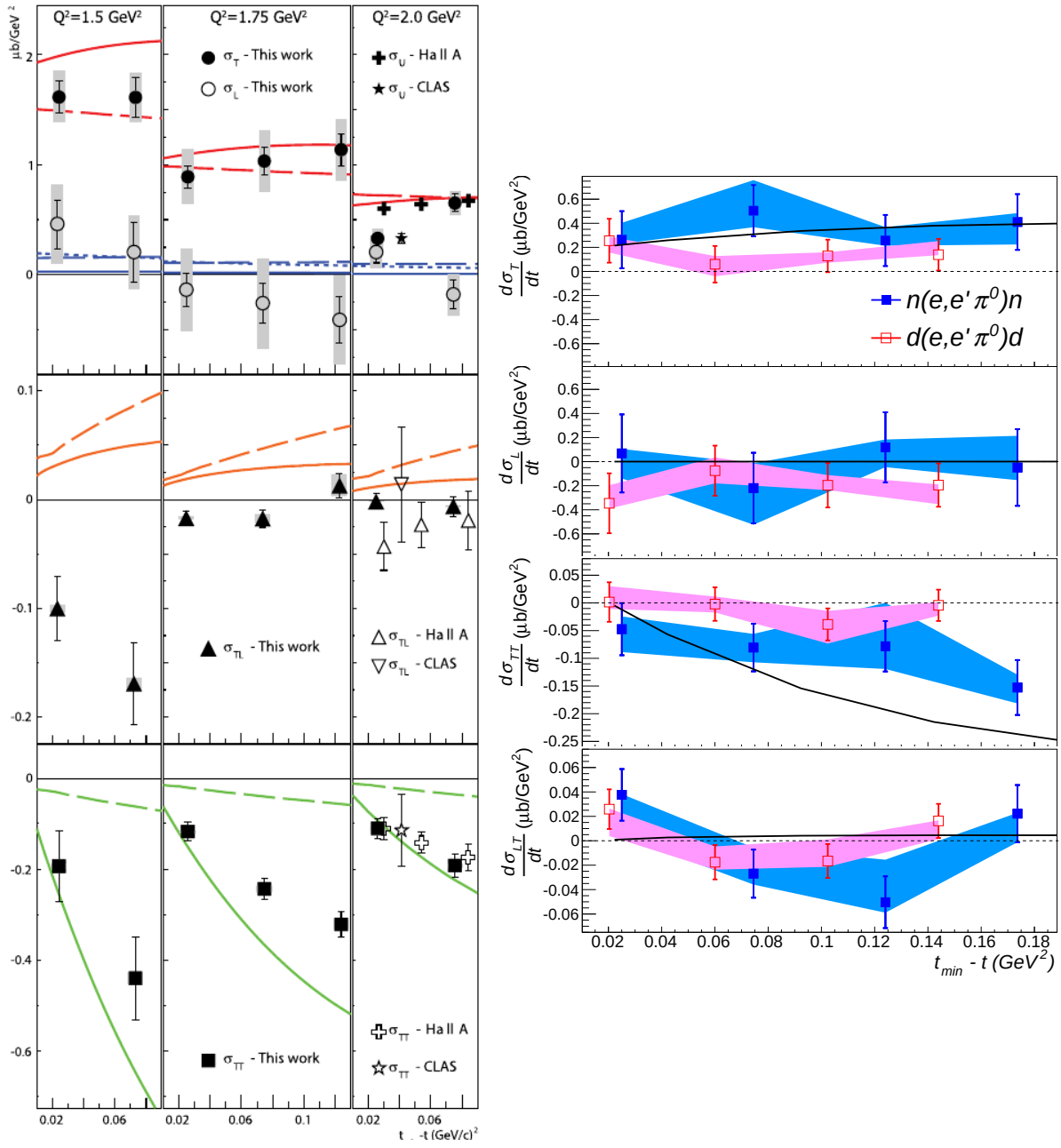

FIG. 18: Rosenbluth separation of the exclusive π^0 cross section off the proton (left) [31] and the neutron (right) [4].

axial-vector current, $\mu_\pi \approx 2$ GeV (at a scale of 2 GeV). This would suggest that there is no strong suppression of the transverse amplitudes at values of Q^2 accessible in present-day experiments. It is thus of great interest to determine the relative longitudinal and transverse contributions to the exclusive π^0 cross section.

This Rosenbluth separation of the π^0 electroproduction cross section off the proton will be done as part of the approved experiment E12-13-010. The run on an LD_2 target proposed herein will allow to perform this L/T separation also in the case of a quasi-free neutron target. This was done in experiment E08-025 [4] at 6 GeV and $x_B = 0.36$, but it is currently not yet planned in the kinematics enabled by the 12 GeV upgrade of CEBAF.

VII. SUMMARY AND BEAM TIME REQUEST

We propose to measure the cross section of the DVCS reaction off quasi-free neutrons accurately in a wide range of kinematics allowed by a set of beam energies up to 11 GeV. We will exploit the azimuthal angle, beam-energy and helicity dependence of the cross section to extract the complete set of observables from an unpolarized quasi-free neutron target. It is well established that the electron beam-helicity dependence of the cross section is dominated by the $\Im$m part of the DVCS†BH interference. In addition, we demonstrated in [1] that the electron beam-energy dependence of the cross section can be used to disentangle the $|\text{DVCS}|^2$ and $\Re$e[DVCS†BH] contributions. The combination of neutron and proton data is required to separate the up-and down-flavor dependence of the nucleon GPDs.

We plan to use the Hall C High-Momentum Spectrometer (HMS) combined with the high resolution $PbWO_4$ calorimeter of the Neutral Particle Spectrometer (NPS) facility. This is the exact same experimental equipment as approved experiment E12-13-010, which has already passed its Experiment Readiness Review (ERR) at Jefferson Lab and is currently scheduled to run in 2023–2024.

In order to complete this full mapping of the flavor dependence of GPDs over a wide range of kinematics, we request 44 days of longitudinally polarized electron beam ($\mathcal{P} > 75\%$, with transverse polarization limited to only a few percent) on a 10 cm LD_2 target. LD_2 running will be optimally interleaved with the approved LH_2 program to reduce systematic uncertainties.

REFERENCES

[1] M. Defurne et al., Nature Commun. **8**, 1408 (2017), 1703.09442.
[2] F. Georges et al. (Jefferson Lab Hall A) (2022), Phys. Rev. Lett., in press, 2201.03714.
[3] M. Benali et al., Nature Phys. **16**, 191 (2020).
[4] M. Mazouz et al. (Jefferson Lab Hall A), Phys. Rev. Lett. **118**, 222002 (2017), 1702.00835.
[5] D. Müller, D. Robaschik, B. Geyer, F. M. Dittes, and J. Horejsi, Fortschr. Phys. **42**, 101 (1994), hep-ph/9812448.
[6] X. Ji, Phys. Rev. **D55**, 7114 (1997), hep-ph/9609381.
[7] X. Ji, Phys. Rev. Lett. **78**, 610 (1997), hep-ph/9603249.
[8] X.-D. Ji, W. Melnitchouk, and X. Song, Phys. Rev. D **56**, 5511 (1997), hep-ph/9702379.
[9] A. V. Radyushkin, Phys. Rev. **D56**, 5524 (1997), hep-ph/9704207.
[10] A. V. Radyushkin, Phys. Lett. B **380**, 417 (1996), hep-ph/9604317.
[11] J. C. Collins and A. Freund, Phys. Rev. D **59**, 074009 (1999), hep-ph/9801262.
[12] X. Ji and J. Osborne, Phys. Rev. **D58**, 094018 (1998), hep-ph/9801260.
[13] A. V. Belitsky, D. Müller, and A. Kirchner, Nucl. Phys. **B629**, 323 (2002), hep-ph/0112108.
[14] M. Burkardt (2007), 0711.1881.
[15] O. V. Teryaev, in *11th International Conference on Elastic and Diffractive Scattering* (2005), hep-ph/0510031.
[16] I. V. Anikin and O. V. Teryaev, Phys. Rev. D **76**, 056007 (2007), 0704.2185.
[17] I. V. Anikin and O. V. Teryaev, Fizika B **17**, 151 (2008), 0710.4211.
[18] M. Diehl and D. Y. Ivanov, in *12th Workshop on High Energy Spin Physics* (2007), pp. 89–93, 0712.3533.
[19] M. V. Polyakov and C. Weiss, Phys. Rev. D **60**, 114017 (1999), hep-ph/9902451.
[20] M. Mazouz et al. (Jefferson Lab Hall A Collaboration), Phys. Rev. Lett. **99**, 242501 (2007), 0709.0450.
[21] M. Lacombe et al., Phys. Rev. **C21**, 861 (1980).
[22] M. Vanderhaeghen, P. A. M. Guichon, and M. Guidal, Phys. Rev. Lett. **80**, 5064 (1998).
[23] M. Vanderhaeghen, P. A. M. Guichon, and M. Guidal, Phys. Rev. D **60**, 094017 (1999).
[24] F. Cano and B. Pire, Eur. Phys. J. **A19**, 423 (2004).
[25] G. R. Goldstein, J. O. Gonzalez Hernandez, and S. Liuti, Phys. Rev. **D84**, 034007 (2011), 1012.3776.
[26] G. R. Goldstein, J. O. Gonzalez Hernandez, and S. Liuti, Phys. Rev. **D91**, 114013 (2015), 1311.0483.
[27] M. Diehl, T. Gousset, B. Pire, and J. P. Ralston, Phys. Lett. **B411**, 193 (1997), hep-ph/9706344.
[28] A. Belitsky and D. Müller, Phys. Rev. **D82**, 074010 (2010), 1005.5209.
[29] E. Fuchey et al., Phys. Rev. C **83**, 025201 (2011), 1003.2938.
[30] I. Bedlinskiy et al. (CLAS), Phys. Rev. Lett. **109**, 112001 (2012), 1206.6355.
[31] M. Defurne et al. (Jefferson Lab Hall A), Phys. Rev. Lett. **117**, 262001 (2016), 1608.01003.
[32] J. C. Collins, L. Frankfurt, and M. Strikman, Phys. Rev. **D56**, 2982 (1997), hep-ph/9611433.
[33] S. J. Brodsky and G. R. Farrar, Phys. Rev. Lett. **31**, 1153 (1973).
[34] S. Ahmad, G. R. Goldstein, and S. Liuti, Phys. Rev. D **79**, 054014 (2009), 0805.3568.
[35] S. V. Goloskokov and P. Kroll, Eur. Phys. J. A **47**, 112 (2011), 1106.4897.
[36] P. Hoodbhoy and X. Ji, Phys. Rev. **D58**, 054006 (1998), hep-ph/9801369.
[37] M. Diehl, Eur. Phys. J. C **19**, 485 (2001), hep-ph/0101335.